Journal of Engineering Science and Technology
Vol. 21, No. 3 (2026) 812 - 835

MASS TRANSPORT BEHAVIOUR OF CU(II) REMOVAL FROM AQUEOUS SOLUTION USING JATROPHA OIL BIOBASED COMPOSITE MEMBRANE

NUR HANINAH HARUN[1], ZURINA ZAINAL ABIDIN[2,*], MOHAMAD REZI ABDUL HAMID[2], MOHD YUSOF HARUN[2], SOH MING LUN[2], ABDUL HALIM ABDULLAH[3], RIZAFIZAH OTHAMAN[4]

[1]Faculty of Chemical and Energy Engineering, Universiti Teknologi Malaysia, Skudai, 81310, Johor, Malaysia
[2]Department of Chemical and Environmental Engineering, Faculty of Engineering, Universiti Putra Malaysia, Serdang, 43400, Selangor, Malaysia
[3]Department of Chemistry, Faculty of Science, Universiti Putra Malaysia, Serdang 43400, Selangor, Malaysia
[4]Department of Chemical Science and Food Technology, Universiti Kebangsaan Malaysia, Bangi 43600, Selangor, Malaysia
*Corresponding Author: zurina@upm.edu.my

Abstract

Rising concerns over heavy metal pollution drive the use of eco-friendly membrane like Jatropha oil/graphene oxide and understanding the mass transfer behaviour is vital for efficient performance. *Jatropha* oil/graphene oxide composite membrane under low loading (JPU/GO 0.50 wt%) has been produced for aqueous Cu(II) removal. During filtration, the concentration adjacent to the membrane exceeds that of the bulk solution, hence forming a concentration profile that is caused by the mass transport behaviour. Therefore, investigating the mass transfer coefficient will assist in understanding fouling phenomena. Thus, this work aims to elucidate the transport behaviour of the JPU/GO membrane that provides a comprehensive framework to predict the membrane performance using combined film theory/solution-diffusion (CFSD) and combined film theory/Spiegler-Kedem (CFSK). Copper sulphate solubility data in water was used to regress pair interaction parameters in Aspen Plus to compute activity coefficients using the eNRTL model. The obtained activity coefficients were then employed to determine the osmotic pressure to estimate CFSD and CFSK parameters for model fittings. The experimental and the predicted data for the CFSD and CFSK models were compared and were determined to be in strong concordance with high R^2 values (> 0.9). For a diagnostic test, residual plots were conducted in which the residual error from the CFSK model was lower than the CFSD model, indicating that the CFSK model demonstrated a better prediction than the CFSD model. Consequently, the CFSK model was determined to be the most suitable mass transfer model for characterising the mass transfer correlation of a JPU/GO 0.50 wt% membrane in the elimination of Cu(II).

Keywords: Activity coefficient, Mass transfer, Membrane filtration, Water treatment.

1. Introduction

Both developed and developing countries are facing water pollution problems, including accidental leaching of metal ions [1, 2]. Heavy metals such as cobalt, nickel, and cadmium pose considerable health risks, like cancer and internal organs failure [3, 4]. Various methods have been employed for wastewater remediation, including membrane filtration [5, 6]. Membrane filtration is frequently favoured due to its operational simplicity, ease of handling, and minimal environmental impact [7]. Filtration generally involves the use of a thin, semi-permeable barrier that selectively permits specific species to traverse while excluding unwanted substances, driven by an applied force and its efficiency relies largely on the membrane's porosity and selectivity.

In recent years, the use of biopolymers in membrane fabrication has garnered increasing attention as part of the global shift toward sustainable and environmentally friendly technologies. Biopolymers can be synthesised either from monomers or through the chemical modification of natural polymers such as polylactic acid (PLA), cellulose and vegetable oils [8-12]. Notably, vegetable oils have emerged as promising renewable feedstocks for biomaterial synthesis, offering sustainability and widespread natural availability.

As reported, soybean oil-based polyurethane with nanocellulose from pineapple leaves composite has managed to remove dyes from aqueous solution [13], while nyamplung oil-based polyurethane has been used to filter mercury from aqueous solution [14]. However, the use of vegetable oil-based nanocomposite membranes specifically for heavy-metal ion removal remains limited. Most vegetable oil-based polymer incorporate with nanoparticle studies focus on dye removal, antifouling coating resistance, and oil – water separation [14-16], relatively few reported on solid vegetable oil-based nanocomposite membranes targeted at heavy-metal ion removal.

Jatropha oil unique chemical composition has positioned it as a valuable resource in polymer technology. It contains a high proportion of unsaturated fatty acids, specifically oleic acid (41.68%) and linoleic acid (35.55%) which facilitate further chemical modifications [17, 18]. Jatropha oil undergoes epoxidation followed by ring-opening to yield polyols containing hydroxyl groups, which subsequently react with hexamethylene diisocyanate (HDI) to form the polyurethane network [19]. In this structure, Jatropha oil serves as a renewable source of polyols, contributing polyester-based soft segments derived from triglyceride ester linkages that enhance flexibility and toughness. The aliphatic hard segments introduced by HDI complement this by providing rigidity and structural stability, resulting in a balanced polyurethane backbone suitable for membrane applications.

Beyond technical advantages, the adoption of vegetable oil-based polymers supports the United Nations' Sustainable Development Goals (SDGs), specifically responsible consumption and production (SDG 12), conservation of aquatic ecosystems (SDG 14), and protection of terrestrial resources (SDG 15). Despite these advantages, previous studies showed that while membranes derived from vegetable oils are considered promising but still suffer from poor material properties that reduce filtration efficiency due to suboptimal morphology and chemical structure [19].

As reported in our earlier work, pristine JPU membranes exhibited relatively hydrophobic behaviour, with a contact angle of 88.8°, and lacked sufficient active

functional groups to facilitate solute interactions [19]. To address these limitations, membranes are frequently modified with nanoparticles, to enhance selectivity and reduce fouling [20]. Furthermore, new insights into transport mechanisms, its connection to membrane composition and filtration performance is imperative.

Graphene oxide (GO) is widely used in material science, nanotechnology, biomedicine and wastewater [21-25]. It is employed as a membrane additive in composite products owing to its distinctive structure and surface properties. The presence of hydroxyl and carboxyl groups on the graphene oxide surface are adept at adsorbing metal cations [26].

In our recent work, bio-based Jatropha polyurethane membranes were fabricated with varying GO content (0.35, 0.5, and 0.65 wt%), with 0.50 wt% GO (JPU/GO 0.50 wt%) identified as the optimum composition [19]. The incorporation of GO decreased the contact angle of JPU membranes from 88.8° (pristine JPU) to 52.1° at 0.50 wt% GO, making it the most hydrophilic sample. This cooperative effect between JPU and GO improved both water transport and Cu(II) rejection, with performance enhanced from 50% to 71%.

As demonstrated in our earlier work using the optimum JPU/GO 0.50 wt% membrane [19], the rejection of Cu(II) ions is governed by charge-ion interactions. At increasing electrolyte concentrations, the membrane charge density rises due to complexation and adsorption of ions on the membrane surface or within the pore walls. However, at higher feed concentrations, excess solute accumulation leads to concentration polarization and higher osmotic pressure, resulting in reduced rejection efficiency or fouling. These findings highlight the mechanistic role of the JPU/GO 0.50 wt% membrane in balancing surface charge effects with mass transfer limitations during heavy metal removal.

Studying the mass transport coefficient could aid in understanding the fouling phenomena given that the hydrodynamics of the filtration system substantially influences the solute mass transport on the concentration polarisation (CP) layer, which can be represented by film theory model. Transport behaviour is generally described by three models: (i) Solution-Diffusion (non-porous), (ii) pore-flow (porous), and (iii) Spiegler-Kedem (irreversible thermodynamics) [27]. The solution-diffusion (SD) model assumes transport through polymer chain interstices, while the pore-flow model considers transport through pores by diffusion and convection.

In contrast, the Spiegler–Kedem (SK) model is widely used to describe transport behaviour when membrane structure is not fully characterized [26]. Because no pores were observed on the membrane top skin layer (Section 3.1), the solution-diffusion model was selected. The Spiegler–Kedem model was also applied for comparison, as it is widely used to describe transport behaviour when membrane structure is not fully characterized. Accordingly, two mass transfer models were employed: the combined film theory/solution-diffusion (CFSD) and combined film theory/Spiegler-Kedem (CFSK) models.

Since the exact membrane transport mechanisms are not well comprehended, hence thermodynamic model [26] can be used as an alternative approach. In general, the mass transfer coefficient, k, represents the relationship among the feed flow rate, solute properties, and the membrane system [28]. Sherwood correlation is widely adopted to assess transport behaviour. It assumes that membrane functions as an impermeable, smooth barrier that excludes solute movement over the membrane [25]. In this research, k was calculated using the solution-diffusion

model alongside the irreversible thermodynamics-based Spiegler-Kedem (SK) model to address this limitation.

The irreversible thermodynamic model posits that membrane transport transpires by a mix of diffusion and convection. This method treats the membrane as a "black box," indicating that extensive knowledge of its internal structure or porosity is unnecessary for the analysis [26]. The SK model is commonly used to explain the membrane transport behaviour when the membrane structure is not fully explored due to its simplified assumption on the membrane structure, which requires no inclusion of membrane characteristics, thus significantly decreasing the numerical complexity and the computation efforts [29].

Additionally, mass transfer models are established by fundamental equations that take into consideration the mass balance and transport of solvent and solute based on pressure and concentration gradient, respectively. The separation process entails the buildup of solutes on the membrane surface; therefore, CP is incorporated into the equations based on film theory [30].

While CFSD and CFSK models have been used in membrane transport studies, they have not been applied to vegetable oil-based polymeric nanocomposites for water treatment. By examining this system, our work provides a clearer view of how such green materials function during filtration and highlights their potential to advance the design of bio-based membranes, offering new opportunities for more sustainable water treatment technologies. Therefore, this work aims to study the transport behaviour of the JPU/GO 0.50 wt% membrane by considering the non-ideality effects of the electrolyte (represented by the Cu(II) feed solution) [31] through calculation of the activity coefficient and osmotic pressure. Later membrane transport mechanisms were elucidated by CFSD and CFSK.

2. Material and Methods

2.1. Materials

The raw materials and chemicals were sourced from the following companies as listed in Table 1.

Table 1. Sources of raw materials and chemicals.

Raw Materials and Chemicals	Company Name / Brand
Crude Jatropha oil	Bionas Sdn Bhd
Glacial acetic acid	Fisher Scientific
Amberlite IR-120	Sigma-Aldrich
Graphene oxide (GO)	
Hexamethylene diisocyanate (HDI)	
30% hydrogen peroxide (H_2O_2)	
Sodium carbonate (Na_2CO_3)	R&M Chemicals
Copper sulfate pentahydrate ($CuSO_4 \cdot 5H_2O$)	
Anhydrous sodium sulfate (Na_2SO_4)	PC Laboratory Reagent

The methodology and full formulation employed for the preparation of the JPU/GO 0.50 wt% membrane has been thoroughly described in prior research [19]. In brief, the ratio for Jatropha oil-based polyol (JOL) and HDI was set at 5:5 (v/v)

with 0.50 wt% GO based on the total polymer content. JOL was first mixed with GO using a sonicator, and the resulting dispersion was then heated and stirred with HDI before being cast into flat-sheet membranes. Based on the thermal-induced phase separation (TIPS) method, the membranes were subsequently cured at 150 °C. The obtained JPU/GO 0.50 wt% membrane film was then exfoliated using a spatula. The membrane efficacy is commonly determined in terms of its flux and rejection as shown below [30]:

$$J_v = \frac{Q}{A.\Delta t} \tag{1}$$

where J_v (L/m²·h) is the water flux, Q (L) is the permeate, A (m²) is the effective membrane area, and Δt is the duration time (hr). The applied pressure (1.5 bar), feed pH (pH 5), membrane effective area, and operating temperature were maintained throughout all filtration runs for consistency. Only the feed concentration of Cu(II) was varied to study its effect on mass transfer and rejection performance.

Concentration gradient across the feed stream and the permeate stream was observed to obtain the rejection (R_o), while the true rejection (R) may be acquired by substituting the bulk concentration (C_b) with solute concentration at the membrane interface (C_m). Both can be expressed as in Eqs. (2) and (3), respectively [30]:

$$R_o = 1 - \frac{C_p}{C_b} \tag{2}$$

$$R = 1 - \frac{C_p}{C_m} \tag{3}$$

2.2. Membrane characterizations

Nitrogen adsorption isotherms (at 77 K) were obtained using Micrometrics ASAP 2020. The membrane was weighed (0.13 g) and cut into small fragments for sample preparation. The Brunauer-Emmett-Teller (BET) model was used to calculate the specific surface area (S_{BET}), while the non-linear density functional theory (DFT) model was used to establish the pore size distribution.

The surface structure of the membrane was evaluated using the FEI NOVA NANOSEM 230 model at an operational voltage of 20 kV. The membrane specimen was coated with titanium via a sputter coater before imaging to enhance conductivity (Emitech, K550X, UK). The coated membrane sample was mounted on a specimen stub, and the electron images of the samples were collected under low (100x) and high (10,000x) magnifications.

2.3. Convergence test

Transport parameters for CFSD and CFSK models, such as solute permeability (P_s and P_m), mass transfer coefficient (k), and reflection coefficient (σ), are estimated from non-linear parameter estimation Excel Solver. The data used for the estimation are R_o and J_v recorded at varied feed concentrations. A least-squares-based objective function is used for the criterion minimisation:

$$\sum_{i=1}^{n}(y_i - \bar{y}_i)^2 \tag{4}$$

In this equation, y_i is the experimental rejection and $\bar{y}_i$ is the magnitude of the computed rejection. The solver employs the Generalised Reduced Gradient algorithm (GRG), recognised as a highly effective method for nonlinear programming method. This phenomenon is identified as the convergence test.

2.4. Estimation of activity coefficients and osmotic pressure

A major constraint often observed in the pressure-driven filtration process is associated with osmotic pressure, which can be calculated from the VHE (Eq. (5)), and subsequently used to evaluate the system parameters (e.g. water flux and rejection performance) [31].

$$\pi = nCRT \tag{5}$$

where n is a dimensionless Van't Hoff factor, C is the solution molar concentration (mol/L), R is the universal gas constant (L.bar/mol.K), and T is the ideal temperature (298.15 K).

However, the electrolyte solution is categorised as a non-ideal solution due to the presence of charged species with various interactions and conditions that exist in electrolyte solutions but not in non-electrolyte solutions, such as molecule-ion interactions [32, 33]. Such interactions lead to deviation in electrolyte activity coefficient from the ideal solution even at minimal electrolyte concentrations due to ions interactions through electrostatic forces [34]. Therefore, the osmotic pressure was determined using the activity coefficient of the solutions:

$$\Delta\pi = -\frac{RT}{V_w}\ln a \tag{6}$$

where V_w is the molar volume of water (L/mol), and a is the water activity coefficient.

The osmotic pressure is determined by factoring in the activity coefficient of the solutions, which can be approximated using the eNRTL model (a framework that is widely employed for electrolyte systems) [35]. To estimate the osmotic pressure from the eNRTL model, a few steps of calculation and regression need to be considered: i) data regression using solubility data in Aspen Plus to determine the eNRTL model pair parameters, ii) the estimation of the electrolyte activity coefficient at the respective concentration using the eNRTL model equation, and iii) calculating the osmotic pressure using Eq. (6).

2.4.1. Solubility of copper sulfate in water

The solubility data of copper sulfate in water were crucial for estimating the interaction parameters between solvent molecules (water) and electrolyte pairs (copper sulfate) utilised in Aspen Plus data regression [36]. The solubility of copper sulfate in water was ascertained by measuring the mass of the dissolved samples in relation to the volume of water at the corresponding temperature. First, 100 g of water solvent was weighed in beaker *A* at ambient temperature (25 °C).

A total of 500 g of copper sulfate was weighed in another beaker, *B*. Then, copper sulfate from beaker *B* was added bit by bit into the water in beaker *A* and was stirred at the lowest available rpm setting (on a scale 1) until a trace amount of copper sulfate was formed, which indicated the saturation had been achieved. The final weight of copper sulfate in beaker *B* was weighed again to determine the amount of copper sulfate that dissolved in water from beaker *A*. The process was repeated for water temperatures at 50 °C, 80 °C, and 100 °C, respectively.

2.4.2. ASPEN Plus regression data

In the eNRTL model, most of the substances model parameters, such as molecule-electrolyte pair parameters that were used to estimate the electrolyte activity

coefficient, are well-documented in Aspen Plus. Despite this, there were still many unknown parameters for several substances, such as copper sulfate. Hence, a data regression needs to be considered from known experimental data such as solid-liquid equilibrium to generate the required model parameters (pair parameters) [36].

Using the solubility data of copper sulfate in water, the water-copper sulfate interaction parameters were subsequently estimable [36]. To determine the pair parameters for the eNRTL model, the solubility experimental data of copper sulfate was regressed in Aspen Plus, utilising the data regression function. Accurately determining the solvent molecule-electrolyte interaction parameters is essential for modelling electrolyte equilibria in the solvent eNRTL model to ensure reliable parameters.

To perform regression data, an electrolyte simulation model with the ELECNRTL property method was selected. Under the [Components] folder, components in electrolytes were chosen, and [Elec wizard] was selected to identify the chemical reactions in electrolytes. In property methods, the ELECNRTL model is set up. Next, in the [Data] folder, solubility experimental data for copper sulfate in water were entered and named as *D1*. Then, the [Regression] folder was created from the ribbon, and pair parameters were selected (GMELCC, GMELCD, GMELCE, GMELCN) for each molecule-electrolyte pair. By selecting *D1* data, the estimated pair parameters were regressed. The summary of the methodology for ASPEN Plus regression was shown in Fig. 1.

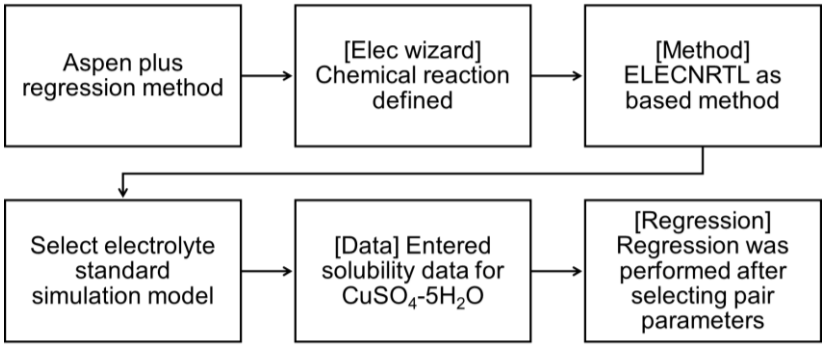

Fig. 1. Methodology chart for determining pair parameters in Aspen Plus.

2.4.3. Electrolyte NRTL model

The eNRTL model delineates the behaviour of the aqueous electrolyte through an excess Gibbs energy expression that incorporates both short-range binary interactions and long-range electrostatic interactions [37]. The long-range electrostatic effects are modelled using the asymmetric Pitzer–Debye–Hückel (PDH) framework, while the short-range interactions are characterized by the NRTL theory. These contributions are mathematically represented in Eq. (7).

$$\frac{G^{ex*}}{RT} = \frac{G^{ex*,PDH}}{RT} + \frac{G^{ex*,lc}}{RT} \tag{7}$$

Similarly,

$$\ln\gamma_i^* = \gamma_i^{*PDH} + \gamma_i^{*lc} \tag{8}$$

where G^{ex*} denotes the total excess Gibbs energy, $G^{ex*,PDH}$ is from the long-range interactions, and $G^{ex*,lc}$ is from the local-range interactions. Here, γ_i^* is the activity coefficient of the electrolyte in water. The PDH is proposed to represent the long-range contribution for molecular and ionic species. This model is adopted the repulsive forces between the ions and expressed as below [38]:

$$\ln\gamma_m^{PDH} = \frac{2A_\emptyset I_x^{3/2}}{1+\rho I_x^{1/2}} \tag{9}$$

$$\ln\gamma_i^{PDH} = -A_\emptyset \left(\left(\frac{2z_i^2}{\rho}\right) ln\left(\frac{1+\rho I_x^{\frac{1}{2}}}{1+\rho I_x^{0\frac{1}{2}}}\right) + \frac{z_i^2 I_x^{\frac{1}{2}} - 2I_x^{\frac{3}{2}}}{1+\rho I_x^{\frac{1}{2}}} - \frac{2I_x (I_x^0)^{\frac{1}{2}}}{1+\rho (I_x^0)^{\frac{1}{2}}}\left(n\frac{\partial I_x^0}{\partial n_i}\right) \right), i = c, a \tag{10}$$

$$A_\emptyset = \frac{1}{3}\left(\frac{2\pi N_A}{v}\right)^{1/2}\left(\frac{Q_e^2}{\in k_B T}\right)^{3/2} \tag{11}$$

$$I_x = \frac{1}{2}\sum_i z_i^2 x_i = \frac{1}{2}\sum_c z_c^2 x_c + \frac{1}{2}\sum_a z_a^2 x_a \tag{12}$$

$$\in = A + B\left(\frac{1}{T} - \frac{1}{C}\right) \tag{13}$$

Table 2 highlights some constants that are present in the equations mentioned.

Table 2. Symbols and its descriptions.

Symbols	Descriptions	Values or units
A	Correlation parameter	78.54
A_Φ	Debye–Hückel parameter	
B	Correlation parameter	31989.4
χ	Ionic strength under the fused salt reference condition	
C	Correlation parameter	298.15
I_x	Ionic strength	mole fraction
k_B	Boltzmann constant	1.3805
N_A	Avogadro's number	
Q_e	Electron charge	4.80298×10^{-10} E.S.U.
v	Molar volume	cm^3/mol
z_a	Charge numbers of the anion	
z_c	Charge numbers of the cation	
z_i	Charge numbers of the species *i*	
ρ	Minimum distance of approach between ions	
ε	Dielectric constant of water	

Equation (10) is then normalised to an infinite dilution reference state to obtain the unsymmetrical model by following the assumption below:

$$I_x^0 = 0 \; and \; \frac{\partial I_x^0}{\partial n_i} = 0, i = c, a \tag{14}$$

The local range contribution was derived from the local composition model of NRTL theory [38]:

$$\frac{G^{ex,lc}}{nRT} = \sum_m n_m \left(\frac{\sum_i X_i G_{im}\tau_{im}}{\sum_i X_i G_{im}}\right) + \sum_c z_c n_c \left(\frac{\sum_{i\neq c} X_i G_{ic}\tau_{ic}}{\sum_{i\neq c} X_i G_{ic}}\right) + \sum_a z_a n_a \left(\frac{\sum_{i\neq a} X_i G_{ia}\tau_{ia}}{\sum_{i\neq a} X_i G_{ia}}\right) \tag{15}$$

$$X_i = C_i x_i = C_i\left(\frac{n_i}{n}\right), i = m, c, a \tag{16}$$

$$n = \sum_i n_i = \sum_m n_m + \sum_c n_c + \sum_a n_a \quad (17)$$

$$G_{ij} = exp(-\alpha_{ij}\tau_{ij}) \quad (18)$$

Table 3 depicts the description of the symbol in the equations above.

Table 3. Symbols and its descriptions.

Symbols	Descriptions
a	Anionic species
c	Cationic species
C_i	Absolute charge number of ionic species and unity for molecular species
m	Molecular species
n_i	Mole number of species *i* in the system
x_i	Mole fraction of species *i* in the system
τ_{ji}	Asymmetric binary interaction energy coefficient
α_{ji}	Non-randomness factor

For a single electrolyte system, two binary parameters, such as adjustable unsymmetric (τ_{ji}) and symmetric parameters (α_{ji}), are associated with the binary electrolyte-molecule pairs. In the eNRTL model, molecules are molecular solvent, *j* (water) and electrolytes are the cation-anion pairs, *i* (Cu^{2+}, SO_4^{2-}). Since τ_{ji} are asymmetric parameters, there are two interaction parameters per binary pair. A Gibbs-Helmholtz-type equation established by Clarke and Glew is offered for the temperature dependence of binary interaction parameters, τ_{ji} [39].

$$\tau_{ij} = A_{ij} + B_{ij}\left(\frac{T}{T} - \frac{T}{T_{ref}}\right) + C_{ij}\left(\frac{T_{ref}}{T} + \ln\frac{T}{T_{ref}}\right) \quad (19)$$

$$\tau_{ji} = A_{ji} + B_{ji}\left(\frac{T}{T} - \frac{T}{T_{ref}}\right) + C_{ji}\left(\frac{T_{ref}}{T} + ln\frac{T}{T_{ref}}\right) \quad (20)$$

Here, A, B, and C can be retrieved from solubility data regression in Aspen Plus. Also, the non-randomness factor, α_{ji} can be obtained from Aspen Plus solubility data regression. The names of the parameters in Aspen Plus are given in Table 4.

Table 4. Pair parameters in Aspen plus regression.

Parameter	Parameter Aspen Plus
A_{ij}, A_{ji}	GMELCC
B_{ij}, B_{ji}	GMELCD
C_{ij}, C_{ji}	GMELCE
α_{ji}	GMELCN

The derivations of the local range contributions model are predicated on a system comprising one fully dissociated liquid electrolyte cation and anion (*c*, *a*) and one solvent *B*. The relevant local-range contributions to the species activity coefficients in aqueous single electrolyte solutions are [38]:

$$\ln\gamma_w^{lc} = \frac{X_c\tau_{cw}G_{cw}+X_a\tau_{aw}G_{aw}}{X_cG_{cw}+X_aG_{aw}+X_w} + \frac{X_cX_a\tau_{wc}G_{wc}}{(X_a+X_wG_{wc})^2} + \frac{X_aX_c\tau_{wa}G_{wa}}{(X_c+X_wG_{wa})^2} - \frac{X_cX_w\tau_{cw}G_{cw}+X_aX_w\tau_{aw}G_{aw}}{(X_cG_{cw}+X_aG_{aw}+X_w)^2} \quad (21)$$

$$\frac{1}{Z_c}\ln\gamma_c^{lc} = \frac{{X_w}^2\tau_{cw}G_{cw}}{(X_cG_{cw}+X_aG_{aw}+X_w)^2} + \frac{X_aX_w\tau_{wa}G_{wa}}{(X_c+X_wG_{wa})^2} + \frac{X_w\tau_{wc}G_{wc}}{X_a+X_wG_{wc}} \quad (22)$$

$$\frac{1}{Z_a}\ln\gamma_a^{lc} = \frac{{X_w}^2\tau_{aw}G_{aw}}{(X_cG_{cw}+X_aG_{aw}+X_w)^2} + \frac{X_cX_w\tau_{wc}G_{wc}}{(X_a+X_wG_{wc})^2} + \frac{X_w\tau_{wa}G_{wa}}{X_a+X_wG_{wc}} \quad (23)$$

The unsymmetric activity coefficients with the aqueous phase infinite dilution reference state then are:

$$\ln\gamma_i^{*lc} = \ln\gamma_i^{lc} - \ln\gamma_i^{lc,\infty},\ i = c, a \quad (24)$$

Thus,

$$\ln\gamma_i^{lc,\infty} = \tau_{wi} + G_{iw}\tau_{iw},\ i = c, a \quad (25)$$

2.5. Theory and model equations

The osmotic pressure obtained from the Van't Hoff equation (VHE) and the eNRTL model were compared and used for subsequent transport model calculation. Two models based on membrane surface morphology studies: the combined film theory/solution-diffusion model (CFSD) and the combined film theory/Spiegler-Kedem model (CFSK) were employed [40-42].

2.5.1. Combined film/theory/solution-diffusion model (CFSD)

The theory of the non-porous models is the transport of the component due to the concentration gradient as the permeant component dissolves within the membrane and is molecularly diffused through the membrane [40]. Also, this model has assumed the equilibrium and steady-state condition is attained within the membrane. This theory is significant as it highlights the method of separation and inferring the membrane's performance using appropriate parameters.

The solution-diffusion model serves as the principal framework for elucidating the transport phenomena in non-porous membranes. This model is extensively applied in various permeation processes, including dialysis, reverse osmosis, forward osmosis, gas separation, and pervaporation, owing to its straightforward equation structure [41]. CP that is caused by the solute retention when filtering through a membrane is incorporated into the equations derived from film theory [30]. Therefore, based on these assumptions, the mass transfer mechanism can be represented by the CFSD model as follows:

$$\frac{R_o}{1-R_o} = \left(\frac{J_v}{P_s}\right) exp\left(\frac{-J_v}{k}\right) \quad (26)$$

From Eq. (5), $\frac{R_o}{1-R_o}$ and J_v parameters can be obtained from the experiment. Therefore, from R_o and J_v experimental data, solute transport parameter (P_s) and k can finally be determined by using non-linear parameter estimation method.

2.5.2. Combined film theory/Spiegler Kedem model (CFSK)

The SK model defines membrane transport as a combination of diffusion and convection. To be precise, the diffusion has resulted from the concentration gradient (dC/dx), while convection is from the applied transmembrane pressure (ΔP). Furthermore, the SK model has been extensively recommended, as it involves fewer membrane parameters, making the method more approachable [42]. This theory model is important to project the efficacy of pressure-driven membrane

filtration concerning rejection rate and water flux assessment to enhance comprehension of membrane separation dynamics [26, 43].

Likewise, after including the effect of CP in the transport equation, the mass transfer mechanism is portrayed by CFSK as follows:

$$\frac{R_O}{1-R_O} = \frac{\sigma}{1-\sigma}\left[1 - exp\left(-J_v\left(\frac{1-\sigma}{P_M}\right)\right)\right]\left[exp\left(\frac{-J_v}{k}\right)\right] \quad (27)$$

Likewise, $\frac{Ro}{1-Ro}$ and J_v can be determined from the experiment. Thus, P_m, σ, and k can be estimated by using a nonlinear parameter estimation method.

3. Results and Discussion

3.1. Membrane characterization and model selection

The BET analysis yielded the membrane's surface area and micropore volume at 10.92 m²/g and 1.06 cm²/g, respectively. As shown in Fig. 2(a), The pore diameter was 0.19 µm, as determined by a non-linear density functional theory (DFT) model of the pore size distribution. However, due to the presence of membrane pores within the cross-section as reported in the previous work [16], these pore size distributions are not reflecting the surface membrane pore size, which can be observed from the adsorption-desorption isotherm as in Fig. 2(b).

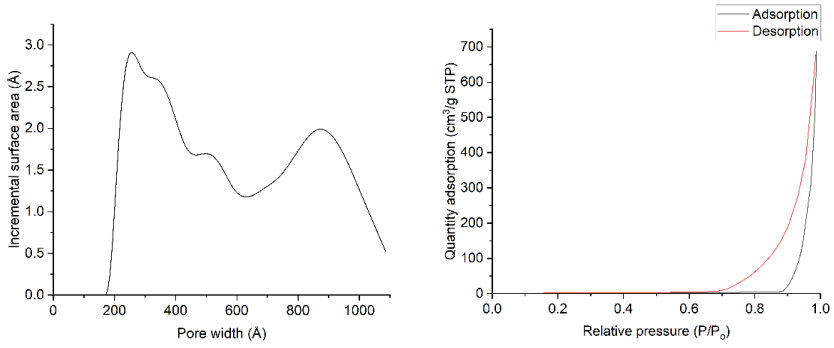

(a) **(b)**

Fig. 2. (a) Pore size distribution calculated by the non-linear DFT model and (b) N_2 adsorption isotherm of the JPU/GO 0.50 wt% membrane.

Isotherms in gas-solid systems for surface area and pore size analysis can be divided into six styles (I to IV), and their hysteresis mode can be categorised into six groups (H1-H4), as shown in Fig. 3 [44]. In accordance with the International Union of Pure and Applied Chemistry (IUPAC) classification, the JPU/GO 0.50 wt% membrane can be classified as a type III isotherm style with type H1 of hysteresis loops mode. In the instance of a type III isotherm, there is a negligible increase in adsorption from the initial to the final stages of gas adsorption, resulting in the absence of discernible monolayer formation.

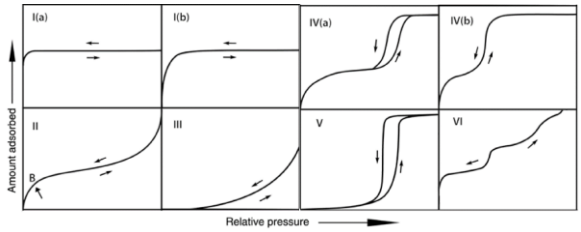

(a)

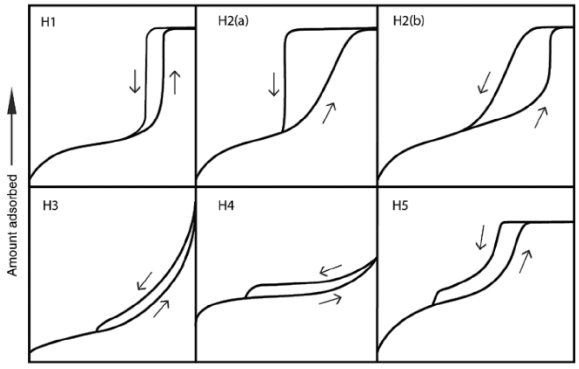

(b)

Fig. 3. (a) adsorption isotherm types and (b) the classification of hysteresis loops Adapted from [46].

Consequently, the adsorbent-adsorbate interactions are comparatively feeble, with the molecules adsorbed and accumulated around the most favourable sites on the non-porous or macroporous solid surface [44]. Hence, the quantity of adsorbed material stays limited at the saturation pressure (i.e., at $p/p_o=1$). For the hysteresis loop (the lag between adsorption/desorption), the observed steep and narrow loop in this study, akin to the type H1 loop, is a definitive indicator of prolonged deposition on the adsorption branches, indicating that the material possesses a restricted range of mesopores. However, with less availability to examine the local membrane pore radius, it is difficult to determine the pore at a lower range (<2 nm).

In addition to supporting the BET analysis, a field emission scanning electron micrograph (FESEM) image of the JPU/GO 0.50 wt% membrane surface was captured as presented in Fig. 4. Based on the results, the JPU/GO 0.50 wt% membrane was assumed to have a dense top surface, as no visible pore was observed.

Therefore, based on the findings obtained from BET and FESEM, the SD model was proposed to elucidate the mechanism of membrane transport. Despite this, the question of whether the membrane is truly homogenous (no pores) or has very tight pores is still a common issue among researchers [27].

As reported by other authors, the transition mechanisms between diffusion and diffusion/convection mechanisms can occur from a 5 Å pore diameter, in which a very slightly "loose" pore that may exist can lead to different main transport behaviours [30, 45].

In this work, SK model analysis was conducted as a comparative study with the SD model. Although with less availability to examine the membrane pore diameter in that range, this still allows one to analyse using SK models since pore diameter data is not required. Furthermore, the SK model has been extensively recommended, as it involves fewer membrane parameters, making the method more simplified and approachable [42].

In addition, the relevance of film theory is underscored in this investigation, particularly in relation to the phenomenon of CP, a prevalent aspect of the filtration process [30]. After considering the aspects necessary for the mathematical model, the membrane transport mechanisms were described by these two models: the CFSD model and the CFSK model.

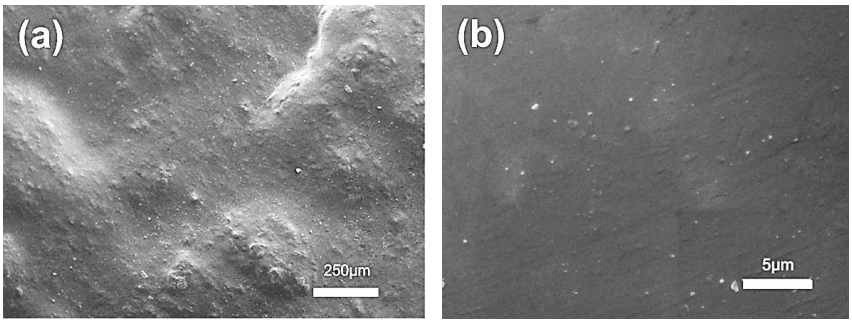

Fig. 4. Electron micrographs of the top surface of JPU/GO 0.50 wt% membrane under (a) 100x magnification (b) 10000x magnification.

3.2. Estimation of activation coefficient and osmotic pressure

The estimated value of osmotic pressure at different feed concentrations was calculated by considering the activity coefficient of the solutions. The interaction parameters of the molecular-electrolyte pair in the electrolyte NRTL (eNRTL) model were determined in Aspen Plus by the regression of solubility data of $CuSO_4.5H_2O$ in pure water to determine the value of the activity coefficient. The estimated pair interaction of the molecule-electrolyte pairs was shown in Table 5. The satisfaction of data regressions was indicated by the parameter's standard deviations, correlation matrix, and the sum of squares error.

As shown in Table 6, the standard deviation value for the estimated parameters was satisfied within the normal range (< 20) [36]. While in the parameter correlation matrix, the off-diagonal entries of the matrix signify the extent of correlation between any two parameters. In detail, the value of the correlation coefficient was zero when the parameters were completely independent of each other, while obtaining values around 1.0 or −1.0 would indicate a strong association between the parameters.

In this case, the asymmetric binary parameters for activity coefficient models exhibited a high correlation; thus, the obtained correlation coefficients should be in the range from 1.0 to −1.0. The results given were parallel with the required conditions as shown in Table 6. With the sum of squares error at 3.2312×10^{-21}, the osmotic pressure could be approximated by utilising the estimated solvent molecule–electrolyte pair interaction parameters.

Table 5. H_2O-(Cu^{2+}, SO_4^{2-}) molecule-electrolyte pair interaction parameter.

Parameter	Component *i*	Component *j*	Value	Standard deviation
GMELCC	H_2O	(Cu^{2+}, SO_4^{2-})	23.315	0.118
GMELCC	(Cu^{2+}, SO_4^{2-})	H_2O	−5.637	0.041
GMELCD	H_2O	(Cu^{2+}, SO_4^{2-})	−1344.649	17.370
GMELCD	(Cu^{2+}, SO_4^{2-})	H_2O	−487.478	2.732
GMELCE	H_2O	(Cu^{2+}, SO_4^{2-})	−886.789	4.943
GMELCE	(Cu^{2+}, SO_4^{2-})	H_2O	201.004	1.518
GMELCN	(Cu^{2+}, SO_4^{2-})	H_2O	0.252	0.002

Table 6. Parameter correlation matrix from Aspen Plus data regression.

Parameter	1	2	3	4	5	6	7
1	1.00						
2	−0.94	1.00					
3	−0.45	0.11	1.00				
4	−0.08	0.06	1.73×10^{-10}	1.00			
5	−0.89	0.99	1.56×10^{-9}	1.38×10^{-9}	1.00		
6	0.92	−0.99	−0.08	−0.20	−0.98	1.00	
7	−0.92	0.96	0.17	0.35	0.92	−0.98	1.00

Figure 5 illustrates the osmotic pressure and activity coefficient computed in accordance with the various feed concentrations in this study. Several studies had identified that the activity coefficient decreases with the increase of copper sulfate concentration [47, 48]. In general, at low concentrations, interactions between ions and solvents are predominant compared to interactions among ions themselves. Nevertheless, as feed concentration increases, ion-solvent interactions diminish owing to elevated electrolyte concentrations. The insufficient amount of solvent decreases the ability of the solvent (water) to dissolve the added ions.

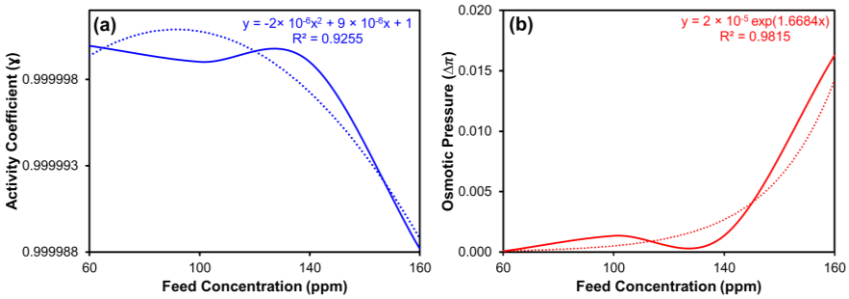

Fig. 5. Estimated (a) activity coefficient and (b) osmotic pressure based on the feed concentrations.

Consequently, the water activity coefficient decreases as the concentration of electrolytes increases. Conversely, osmotic pressure increases as the copper sulfate concentration increases. Higher copper sulfate concentration causes fewer water molecules due to the reduction of available space. As a result, water has a greater tendency to permeate to the opposite side, thus increasing the osmotic pressure. In

summary, higher electrolytes reduce the effective solvent, thus declining the water molecules amount that can dissolve the additional ions [48].

In addition, the applicability of the eNRTL model for osmotic pressure estimation was investigated by determining the relative difference between the osmotic pressure values predicted from the VHE and eNRTL models, as shown in Fig. 6.

From Fig. 6, the VHE forecasts greater osmotic pressure values than the eNRTL model, with a percentage relative difference between the two models remaining below 2%. However, for lower concentrations, the percentage relative differences increase, which indicates the eNRTL model has better osmotic pressure prediction at lower feed concentrations [32]. Given that the concentrations examined in this study are below 140 ppm, Fig. 6(b) demonstrates that the eNRTL model is appropriate for calculating osmotic pressure in permeate flux estimates.

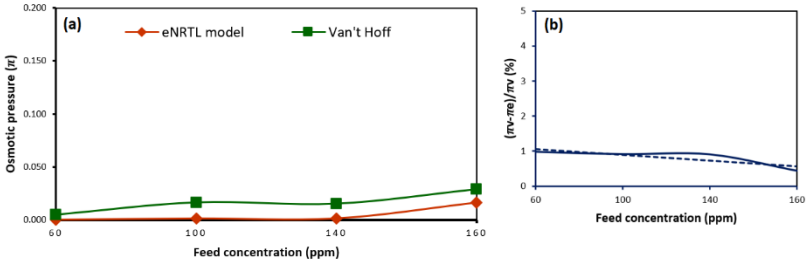

Fig. 6. Comparison (a) osmotic pressure using eNRTL model and VHE with their (b) percentage relative difference.

3.3. Estimation of model parameters

The estimated membrane transport parameters for the CFSD and CFSK models were obtained from a trial-and-error approach using the solver *add-in* function of Microsoft Excel, and the data were tabulated in Table 7. Based on the results, the variation of the solute transport parameters (characterized by P_s *and* P_m) from these two models are almost similar, while the k value varies significantly. This is attributed to the σ values [30, 49, 50], that quantifies the degree of the membrane's semi-permeability, indicating its ability to permit the passage of solvent relative to solute [29].

Table 7. Projected transport characteristics for the JPU/GO 0.50 wt% membrane using the CFSD and CFSK models.

Feed (ppm)	CFSD model		CFSK model		
	P_s (m/s)	$k \times 10^2$ (m/s)	σ	P_m (m/s)	$k \times 10^4$ (m/s)
60	164.45	4.74	0.45	49.10	61.01
100	49.11	4.51	0.72	19.27	54.02
140	56.94	4.30	0.66	29.53	49.71
160	54.75	4.27	0.67	30.18	44.91

In the CFSD model, it is posited that the concentration gradient across the membrane exhibits a strong correlation with the process of diffusive transport [29]. The occurrence of concentration polarisation (CP) can be attributed to the formation of a boundary layer adjacent to the membrane surface at elevated solute

concentrations. In this scenario, the solute concentration within the boundary layer exceeds that of the bulk solution, a phenomenon resulting from the membrane's selective rejection of solutes [47, 48].

As a result, the osmotic pressure at the membrane surface exceeds that of the surrounding solution, thereby diminishing the driving force for solute rejection. This phenomenon subsequently enhances the transport of solutes across the membrane [47, 48]. However, in this work, the obtained solute permeability (P_s) from the CFSD model was not consistent over the operating conditions and was larger than P_m, which was anticipated to be lower due to the diffusive and convective assumption in the CFSK model [30, 32, 51].

In contrast to the CFSD model, convection transport from the CFSK model corresponds to the ionic concentration within the membrane, which can be characterized by σ [52]. The results presented in the table indicate that increased solute rejection corresponds with a higher σ value, demonstrating the CFSK model's high accuracy in predicting membrane transport parameters. Apart from that, since $1-\sigma$ characterises the solute's convective transport, it gives evidence that a lower value signifies an augmentation in the convective ion flux. Therefore, σ is inversely proportional to the permeability solute (P_m) the CFSK model, which was also reported by other authors [29, 30].

Furthermore, the k value obtained from the CFSK model demonstrates a significantly elevated value relative to the CFSD model. The sensitivity of the k value to the initial transport parameters employed in the model is notably pronounced. The variation in k values observed between the two models can be ascribed to the inclusion of the reflection coefficient, σ, within the CFSK model.

This suggests that the k value is dependent on the particular mass transfer model utilised in the analysis [29]. Moreover, since the reflection coefficient σ (0.45 - 0.72) is noticeably far from unity (< 1), lower retention characteristics were presumed due to the convection transport [29]. Another potential explanation arises from the other equation of $k = D/\delta$, where k value will be affected by the solute diffusivity and the thickness of the concentration boundary layer [29].

The transport system associated with the CFSK model is expected to restrict the proliferation of solutes in proximity to the membrane surface as a result of solute convection processes. Consequently, a lower δ and a higher k value are beneficial [29, 30]. Conversely, it is evident that the k value exhibits an inverse proportionality to the feed concentration within the CFSK model.

The increase in the CP boundary layer leads to a diminished k value. From Fig. 7, the k value for the CFSD and CFSK models is related to feed concentration, as confirmed from the measured permeate flux whereby the k value decreases with decreasing flux due to increasing solute retention at higher feed concentrations [53]. A similar trend was also recorded by other authors [30-32].

These findings highlight that the decline in k reflects the intensification of concentration polarization and fouling at elevated solute concentrations [54, 55]. In our earlier work [19], Cu(II) rejection by the JPU/GO 0.50 membrane was shown to be primarily driven by charge–ion interactions. As electrolyte concentration increases, ion complexation and solutes adsorption on the membrane surface or within its pore walls raise the membrane's charge density.

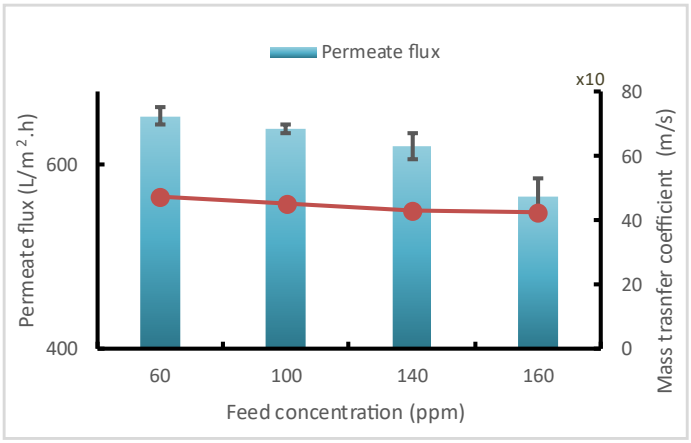

(a)

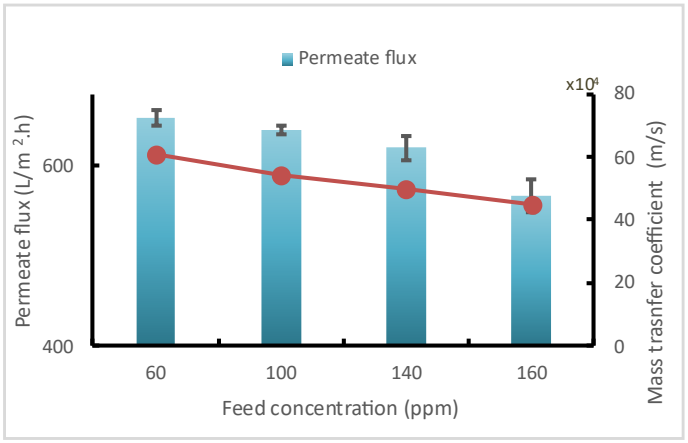

(b)

Fig. 7. Determination of *k* for JPU/GO 0.50 wt% membrane utilizing (a) CFSD and (b) CFSK model (Operating conditions: 1.5 bar and pH 5±0.5).

At higher feed concentrations, excessive solute accumulation leads to concentration polarization and elevated osmotic pressure, which reduce water permeability and promote fouling, thus impact the consistency of membrane performance during prolonged operation. These findings highlight the mechanistic role of the JPU/GO 0.50 membrane in surface charge effects with mass transfer limitations during filtration.

Additionally, while JPU/GO 0.50 wt% membranes exhibit improved hydrophilicity and rejection, their long-term performance may still be challenged by surface solute accumulation, underscoring the need for optimized operating conditions to mitigate fouling effects. Future studies could address these limitations by incorporating antifouling surface modifications or by exploring operational strategies such as periodic backwashing or flow optimization to enhance membrane stability.

3.4. Model validation

To verify the model fitting, the anticipated observed rejection from the CFSD and CFSK models was calculated using the data presented in Table 4. The actual observed rejection (A_o) was then compared with the predicted observed rejection (P_o) as illustrated in Figs. 8(a) and (c). The results indicate that the predicted observed rejection from the CFSD and CFSK models aligns well with the actual data, as evidenced by the high R^2 values. Both models could represent the experimental data; however, the CFSK model demonstrated a higher accuracy in predicting the observed rejection compared to the CFSD model.

This can be observed from the residual plots as shown in Figs. 8(b) and (d), in which the error term is expressed as residuals [53]. From the plotted graph, all the data points from the CFSK model are closely near to zero as compared to the data points from the CFSD model, which indicates lower residual error [46].

This improved agreement is consistent with BET results, which suggested the presence of mesoporous features (<2 nm). Such tight pores, although not visible in FESEM, may facilitate a small degree of convective transport in addition to diffusion, supporting the mechanistic basis for why the CFSK model outperforms the CFSD model in this system. Thus, the CFSK model exhibited superior forecasting capabilities compared to the CFSD model, attributable to its incorporation of an additional convection mechanism rather than relying just on diffusion.

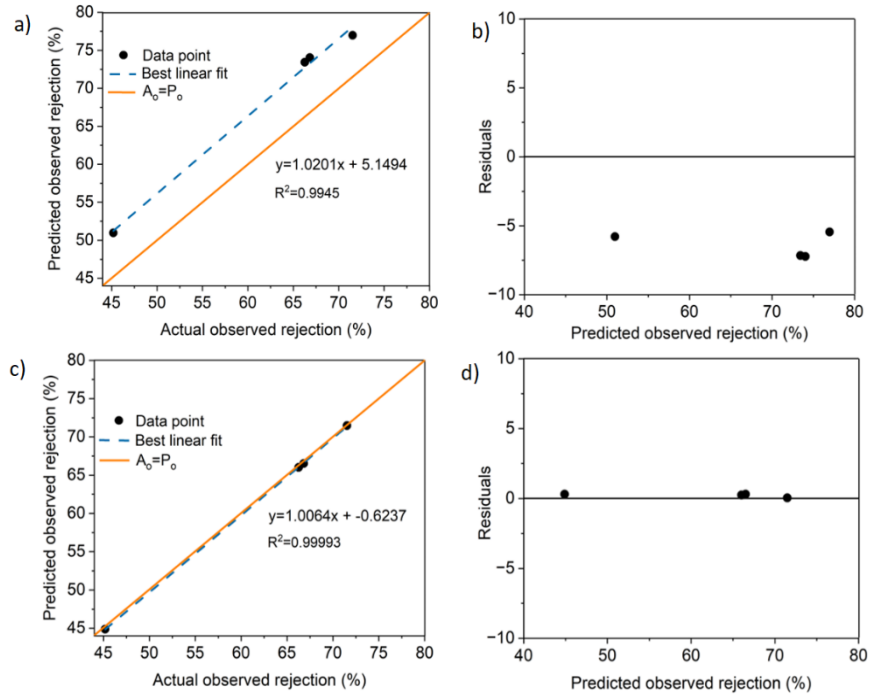

Fig. 8. Predicted versus actual observed rejection and residual plots for (a – b) CFSD and (c – d) CFSK models.

4. Conclusions

The non-ideality of the aqueous single electrolyte, specifically the Cu(II) feed solution, is characterised by the eNRTL model. The molecular-electrolyte interaction parameters within the model were determined using a data regression tool in Aspen Plus, grounded in the solubility data of $CuSO_4 \cdot 5H_2O$ in water as the solvent. The excess Gibbs energy terms have been precisely determined for the water activity coefficient, which was employed to estimate the osmotic pressure of electrolytes across different input concentrations.

The assessment of osmotic pressure was conducted using both eNRTL and VHE. The model fitting results demonstrate that the transport behaviour of the JPU/GO 0.50 wt% membrane for Cu(II) removal is effectively characterised by both CFSK and CFSD models. The theoretical and experimental findings revealed a robust correlation, with the CFSK model yielding more accurate predictions in comparison to the CFSD model. The observed enhancement can be ascribed to the integration of diffusion and convection within the transport mechanisms.

Acknowledgements

We would like to thank the Ministry of Higher Education, Malaysia, under the Fundamental Research Grant Scheme (grant code FRGS/1/2020/TK0/UPM/02/38, project code 03-01- 20-2248FR) and the Initiative Putra Grant (GPI/2022/9720400) for supporting this work.

Nomenclatures

A	Effective membrane area (m^2)
C	Solution molar concentration (mol/L)
C_b	Bulk concentration (mol/L)
C_m	Concentration at the membrane surface (mol/L)
G^*_{ex}	Total excess Gibbs energy
$G^*_{ex,lc}$	Gibbs energy from local range interactions
$G^*_{ex,PDH}$	Gibbs energy from long-range interactions
I_x	Ionic strength (mol/L)
J_v	Water flux ($L/m^2 \cdot h$)
k	Mass transfer coefficient (m/s)
k_B	Boltzmann constant
N_A	Avogadro's number
P_m	Permeability solute (m/s)
P_s	Solute permeability (m/s)
Q	Permeate (L)
Q_e	Electron charge (E.S.U)
R_o	Observed rejection (%)
R	True rejection (%)
t	Duration time (hr)
z_i	Charge number of species i
T	Ideal temperature (K)
V_w	Molar volume of water (L/mol)
v	Molar volume (cm^3/mol)

Greek Symbols

γ	Activity coefficient
γ_w	Water activity coefficient
$\Delta\pi$	Osmotic pressure (bar)
ε_w	Dielectric constant of water
ζ	Nonrandomness factor
λ	Interaction parameter
σ	Reflection coefficient (unitless)

Abbreviations

BET	Brunauer-Emmett-Teller
CFSD	Combined Film Theory/Solution-Diffusion Model
CFSK	Combined Film Theory/Spiegler-Kedem Model
CP	Concentration Polarization
DFT	Density Functional Theory
eNRTL	Electrolyte Non-Random Two-Liquid
FESEM	Field Emission Scanning Electron Microscopy
GO	Graphene Oxide
JPU	Jatropha Polyurethane
NRTL	Non-Random Two-Liquid
PDH	Pitzer-Debye-Hückel
SK	Spiegler-Kedem
VHE	Van't Hoff equation

References

1. United States Environmental Protection Agency. (2009). National water quality inventory: *Report to Congress.* U.S. Environmental Protection Agency, EPA 841-R-16-011.
2. Rowell, R.M.; and Boving, T.B. (2010). *Water filtration using biomaterials.* In Rowell, R.M.; Caldeira, F.; and Rowell, J.K. (Eds.), *Sustainable development in the forest products industry*. UFP Edition, Lisbon, Portugal.
3. Aji, M.P.; Wiguna, P.A.; Karunawan, J.; Wati, A.L.; and Sulhadi. (2017). Removal of heavy metal nickel-ions from wastewaters using carbon nanodots from frying oil. *Procedia Engineering*, 170, 36-40.
4. Prabhu, P.P.; and Prabhu, B. (2018). A review on removal of heavy metal ions from waste water using natural/modified bentonite. *MATEC Web of Conferences*, 144, 02021.
5. Aljohny, B.O.; Ahmad, Z.; Shah, S.A.; Anwar, Y.; and Khan, S.A. (2020). Cellulose acetate composite films fabricated with zero-valent iron nanoparticles and its use in the degradation of persistent organic pollutants. *Applied Organometallic Chemistry*, 34(11), e5892.
6. Yao, Q.; Fan, B.; Xiong, Y.; Jin, C.; Sun, Q.; and Sheng, C. (2017). 3D assembly based on 2D structure of cellulose nanofibril/graphene oxide hybrid aerogel for adsorptive removal of antibiotics in water. *Scientific Reports*, 7(1), 45914.
7. Xu, L.; Zhou, Z.; Graham, N.J.D.; Liu, M.; and Yu, W. (2021). Enhancing ultrafiltration performance by gravity-driven up-flow slow biofilter pre-treatment to remove natural organic matters and biopolymer foulants. *Water Research*, 195, 117010.

8. Ibrahim, S.; Riahi, O.; Said, S.M.; Sabri, M.F.M.; and Rozali, S. (2019). *Biopolymers from crop plants*. In Hashmi, S. (Ed.), *Reference Module in Materials Science and Materials Engineering*. Elsevier.
9. Phan, D.-N.; Khan, M.Q.; Nguyen, N.-T.; Phan, T.-T.; Ullah, A.; Khatri, M.; Kien, N.N.; and Kim, I.-S. (2021). A review on the fabrication of several carbohydrate polymers into nanofibrous structures using electrospinning for removal of metal ions and dyes. *Carbohydrate Polymers*, 252, 117175.
10. Russo, T.; Fucile, P.; Giacometti, R.; and Sannino, F. (2021). Sustainable removal of contaminants by biopolymers: A novel approach for wastewater treatment. Current state and future perspectives. *Processes*, 9(4), 719.
11. Karimi, M.B.; Khanbabaei, G.; and Sadeghi, G.M.M. (2017). Vegetable oil-based polyurethane membrane for gas separation. *Journal of Membrane Science*, 527, 198-206.
12. Ibrahim, S.; Ahmad, A.; and Mohamed, N. (2015). Characterization of novel castor oil-based polyurethane polymer electrolytes. *Polymers*, 7(4), 747-759.
13. Chandrashekhar, A.; Gopi, J.A.; and Prabhu, T.N. (2020). Development of flexible bio-based porous polyurethane nanocellulose composites for wastewater treatment. *Proceedings of the International Conference On Advances In Materials Research* (*ICAMR*-2019), Bangalore, India, 040002.
14. Marlina; Farida, M.; and Mustanir. (2017). Synthesis and characterization of polyurethane membrane from nyamplung seed oils (Calophyllum inophyllum). *Asian Journal of Chemistry*, 29(9), 1912-1916.
15. Nakpong, P.; and Wootthikanikkhan, S. (2010). Optimization of biodiesel production from Jatropha oil (*Jatropha curcas* L.) using response surface methodology. *Kasetsart Journal*: *Natural Science*, 44(2), 290-299.
16. Cheng, Q.; An, X.-P.; Li, Y.-D.; Huang, C.-L.; and Zeng, J.-B. (2017). Sustainable and biodegradable superhydrophobic coating from epoxidized soybean oil and ZnO nanoparticles on cellulosic substrates for efficient oil/water separation. *ACS Sustainable Chemistry & Engineering*, 5(12), 11440-11450.
17. Huang, J.; Sha, G.; Cui, M.; Quan, M.; Wang, Y.; Lu, Y.; Zhu, J.; and Chen, J. (2024). A highly reactive soybean oil-based superhydrophobic polyurethane film with long-lasting antifouling and abrasion resistance. *Nanoscale Advances*, 6(22), 5663-5670.
18. Ong, H.C.; Mahlia, T.M.I.; Masjuki, H.H.; and Norhasyima, R.S. (2011). Comparison of palm oil, Jatropha curcas, and Calophyllum inophyllum for biodiesel: A review. *Renewable and Sustainable Energy Reviews*, 15(8), 3501-3515.
19. Harun, N.H.; Zainal Abidin, Z.; Abdullah, A.H.; and Othaman, R. (2020). Sustainable jatropha oil-based membrane with graphene oxide for potential application in Cu(II) Ion removal from aqueous solution. *Processes*, 8(2), 230.
20. Yin, J.; and Deng, B. (2015). Polymer-matrix nanocomposite membranes for water treatment. *Journal of Membrane Science*, 479, 256-275.
21. Lu, F.; Zhang, S.; Gao, H.; Jia, H.; and Zheng, L. (2012). Protein-decorated reduced oxide graphene composite and its application to SERS. *ACS Applied Materials & Interfaces*, 4(6), 3278-3284.

22. Wang, L.; Zhang, Y.; Wu, A.; and Wei, G. (2017). Designed graphene-peptide nanocomposites for biosensor applications: A review. *Analytica Chimica Acta*, 985, 24-40.
23. Wang, Z.; Colombi Ciacchi, L.; and Wei, G. (2017). Recent advances in the synthesis of graphene-based nanomaterials for controlled drug delivery. *Applied Sciences*, 7(11), 1175.
24. Perreault, F.; Fonseca De Faria, A.; and Elimelech, M. (2015). Environmental applications of graphene-based nanomaterials. *Chemical Society Reviews*, 44(16), 5861-5896.
25. Lee, S.; Amy, G.; and Cho, J. (2004). Applicability of Sherwood correlations for natural organic matter (NOM) transport in nanofiltration (NF) membranes. *Journal of Membrane Science*, 240(1-2), 49-65.
26. Spiegler, K.S.; and Kedem, O. (1966). Thermodynamics of hyperfiltration (reverse osmosis): Criteria for efficient membranes. *Desalination*, 1(4), 311-326.
27. Khalaf, T.Y. (2008). Effect of feed temperature on concentration polarization and efficiency of reverse osmosis systems. *Al-Nahrain Journal for Engineering Sciences*, 11(1), 145-152.
28. Murthy, Z.V.P.; and Gupta, S.K. (1997). Estimation of mass transfer coefficient using a combined nonlinear membrane transport and film theory model. *Desalination*, 109(1), 39-49.
29. Naz Ahmed, F. (2013). *Modified Spiegler-Kedem model to predict the rejection and flux of nanofiltration processes at high NaCl concentrations*. MSc dissertation, Department of Civil Engineering, University of Ottawa.
30. Woldehawariat, B.S. (2010). *Flux and rejection characteristics of amine wastewater using membrane separation processes*. MSc dissertation, Department of Chemical Engineering, Universiti Teknologi Petronas.
31. Nagy, E.; Hegedüs, I.; Rehman, D.; Wei, Q.J.; Ahdab, Y.D.; and Lienhard, J.H. (2021). The need for accurate osmotic pressure and mass transfer resistances in modeling osmotically driven membrane processes. *Membranes*, 11(2), 128.
32. Aspen Technology. (n.d.). *Aspen physical property system: Physical property methods and models V*11.1. Aspen Technology, Inc., Cambridge, MA, USA.
33. Smith, W.R.; Moučka, F.; and Nezbeda, I. (2016). Osmotic pressure of aqueous electrolyte solutions via molecular simulations of chemical potentials: Application to NaCl. *Fluid Phase Equilibria*, 407, 76-83.
34. Thomsen, K. (2009). *Electrolyte solutions*: *Thermodynamics*, *crystallization*, *separation methods.* DTU Chemical Engineering, Technical University of Denmark.
35. Liu, C.; Tang, G.; Ding, H.; Chen, R.; and Liu, M. (2015). Determination of the solubility and thermodynamic properties of wedelolactone in a binary solvent of ethanol and water. *Fluid Phase Equilibria*, 385, 139-146.
36. Kim, K.-I.; Ri, J.-H.; Kim, S.-U.; and Kim, I.-H. (2020). Estimation of interaction parameters of electrolyte NRTL model based on NaCN and Na_2CO_3 solubility in water-ethanol mixed solvent and process simulation for separation of NaCN/Na_2CO_3. *SN Applied Sciences*, 2(12), 2112.

37. Chen, C.-C.; Britt, H.I.; Boston, J.F.; and Evans, L.B. (1982). Local composition model for excess Gibbs energy of electrolyte systems. Part I: Single solvent, single completely dissociated electrolyte systems. *AIChE Journal*, 28(4), 588-596.
38. Hossain, N.; Bhattacharia, S.K.; and Chen, C.-C. (2016). Temperature dependence of interaction parameters in electrolyte NRTL model. *AIChE Journal*, 62(4), 1244-1253.
39. Clarke, E.C.W.; and Glew, D.N. (1966). Evaluation of thermodynamic functions from equilibrium constants. *Transactions of the Faraday Society*, 62, 539.
40. Paul, D.R. (2004). Reformulation of the solution-diffusion theory of reverse osmosis. *Journal of Membrane Science*, 241(2), 371-386.
41. Qian, J.; Yan, R.; Liu, X.; Li, C.; and Zhang, X. (2020). Modification to solution-diffusion model for performance prediction of nanofiltration of long-alkyl-chain ionic liquids aqueous solutions based on ion cluster. *Green Energy & Environment*, 5(1), 105-113.
42. Jain, S.; and Gupta, S.K. (2004). Analysis of modified surface force pore flow model with concentration polarization and comparison with Spiegler-Kedem model in reverse osmosis systems. *Journal of Membrane Science*, 232(1-2), 45-62.
43. Soltanieh, M.; and Gill, W.N. (1981). Review of reverse osmosis membranes and transport models. *Chemical Engineering Communications*, 12(4-6), 279-363.
44. Thommes, M.; Kaneko, K.; Neimark, A.V.; Olivier, J.P.; Rodriguez-Reinoso, F.; Rouquerol, J.; and Sing, K.S.W. (2015). Physisorption of gases, with special reference to the evaluation of surface area and pore size distribution (IUPAC Technical Report). *Pure and Applied Chemistry*, 87(9-10), 1051-1069.
45. Baker, R.W. (2004). *Membrane technology and applications*. John Wiley & Sons, Ltd.
46. Kim, H.-Y. (2019). Statistical notes for clinical researchers: Simple linear regression 3-residual analysis. *Restorative Dentistry & Endodontics*, 44(1), e11.
47. Bockris, J.O.; and Reddy, A.K.N. (1973). *Modern electrochemistry.* Springer New York, NY.
48. Justel, F.J.; Camacho, D.M.; Taboada, M.E.; and Roberts, K.J. (2019). Crystallisation of copper sulfate pentahydrate from aqueous solution in absence and presence of sodium chloride. *Journal of Crystal Growth*, 525, 125204.
49. Ballet, G.T.; Gzara, L.; Hafiane, A.; and Dhahbi, M. (2004). Transport coefficients and cadmium salt rejection in nanofiltration membrane. *Desalination*, 167, 369-376.
50. Murthy, Z.V.P.; and Chaudhari, L.B. (2009). Rejection behavior of nickel ions from synthetic wastewater containing Na_2SO_4, $NiSO_4$, $MgCl_2$, and $CaCl_2$ salts by nanofiltration and characterization of the membrane. *Desalination*, 247(1-3), 610-622.
51. Koyuncu, I.; and Topacik, D. (2003). Effects of operating conditions on the salt rejection of nanofiltration membranes in reactive dye/salt mixtures. *Separation and Purification Technology*, 33(3), 283-294.

52. Szymczyk, A.; and Fievet, P. (2005). Investigating transport properties of nanofiltration membranes by means of a steric, electric, and dielectric exclusion model. *Journal of Membrane Science*, 252(1-2), 77-88.
53. Haan, A.B.D.; Eral, H.B.; and Schuur, B. (2020). *Membrane filtration*. In Haan, A.B.D.; Eral, H.B.; and Schuur, B. (Eds.), *Industrial Separation Processes*. De Gruyter, 359-384.
54. Bose, P.; Dash, S.R.; and Kim, J. (2025). Conductive CuO-CNT/PES membranes for electrochemical membrane filtration and advanced wastewater treatment. *Journal of Water Process Engineering*, 72, 107441.
55. Khor, E.H.; and Samyudia, Y. (2009). The study of mass transfer coefficient in membrane separation for produced water. *International Journal of Chemical Engineering*, 2(2-3), 143-152.